Mechanical Engineering Advances 2025, 3(3), 3621.
doi: https://doi.org/10.59400/mea3621

Article

On supersonic projectile and its special versatile cannon-canister system

Jacob Nagler

Nagler Independent Research Center (NIRC), Haifa 34345, Israel; jacobyan123@gmail.com

CITATION

Nagler J. On supersonic projectile and its special versatile cannon-canister system. Mechanical Engineering Advances. 2025; 3(3): 3621. https://doi.org/10.59400/mea3621

ARTICLE INFO

Received: 8 May 2025
Revised: 7 July 2025
Accepted: 12 July 2025
Available online: 15 September 2025

Abstract: This manuscript presents the design, analysis, and validation roadmap for a compact 20 mm solid-propellant rocket projectile and an associated family of modular launchers optimized for mid-range interception and anti-armor engagement. The system addresses the capability gap between man-portable anti-armor weapons and high-volume point-defense nodes (CIWS). The propulsion architecture utilizes a high-efficiency AP/HTPB (ammonium perchlorate/hydroxyl-terminated polybutadiene) composite grain housed in a selectively laser-melted Inconel 718 pressure casing. Thermal protection is achieved via an integrated polyether ether ketone (PEEK) liner and graphite-phenolic nose, enabling sustained structural integrity against convective and radiative heat fluxes during the 2.5 s burn. Analytic internal-ballistic and nozzle isentropic calculations predict an exit velocity of approximately 1400 m/s (Mach 4) and an under-expanded supersonic jet profile. Terminal-effect models indicate rolled homogeneous armour (RHA)-equivalent penetration near 116 mm and approximately 140 mm into representative composite laminates, exceeding legacy autocannon performance. A compact, mechanically-armed setback primer ensures reliable, self-contained ignition within 6 ms of barrel exit. Three launcher classes are described: soldier-portable shoulder tube, building-mounted multi-tube interceptor, and adaptive variable-barrel arrays, enabling flexible engagement against modern threats such as unmanned aerial vehicle (UAV) swarms and light armor. Finally, the manuscript details a staged experimental validation plan and an environmental compatibility analysis to ensure operational feasibility, safety, and compliance with modern defense standards regarding emissions and handling.

Keywords: miniature rocket projectile; solid propellant; Mach 4; PEEK insulation; Inconel 718; anti-air defense; penetration modeling; launcher systems

1. Introduction

The proliferation of modern battlefield threats, ranging from light armored vehicles to agile unmanned aerial systems (UAS) and saturation rocket salvos has driven an urgent need for versatile, high-speed projectile systems that combine armor penetration, extended range, and operational flexibility [1,2]. As conventional kinetic interceptors such as rapid-fire autocannons and point-defense missile systems face limitations in engagement envelope, cost per shot, and logistical complexity, there is significant motivation to develop compact, scalable solutions that bridge the gap between infantry-deployable weapons and high-volume, installation-based defense nodes [3,4].

Recent advances in solid propulsion materials, nozzle fabrication, and modular launcher architectures have enabled the realization of miniature rocket projectiles

capable of achieving sustained supersonic flight at velocities exceeding Mach 4, while maintaining robust thermal and structural integrity [5, 6]. Within this technological context, the present study introduces and rigorously analyzes a 20 mm rocket-propelled projectile system comprising AP/HTPB monopropellant, Inconel 718 structural elements, and PEEK thermal insulation, integrated across a family of launcher platforms including handheld tubes, rooftop interceptors, and variable-barrel turret arrays.

This work is motivated by the operational need for a platform-agnostic projectile system able to adapt to the dynamic demands of urban anti-air defense, mobile vehicle integration, and flexible point-defense roles against a multitude of aerial and ground-based threats. It targets the following research and engineering aims:

(i) To design and model a high-speed rocket projectile system leveraging optimized grain geometry, advanced nozzle flow dynamics, and thermal protection, demonstrating reliable Mach 4 flight at moderate mass and system cost.

(ii) To quantify and compare penetration, range, and firing rate performance with established anti-tank and anti-air defense solutions, including AT4 HEAT, FIM-92 Stinger, and Phalanx CIWS, contextualizing the operational benefits and limitations of the proposed platform.

(iii) To evaluate modular launcher configurations from soldier-portable to building-mounted multi-tube and variable-barrel interceptors, emphasizing adaptive engagement envelopes, multi-vector attack potential, and manageable power/thermal load.

(iv) To present a comprehensive analytical framework capturing internal ballistics, combustion chamber design, nozzle isentropic flow, and thermal boundary-layer dynamics, thus informing future development of scalable point-defense technologies.

Early generations of shoulder-fired rocket systems, typified by the M136 AT4 and RPG-7, prioritized armor penetration or HE-fragmentation effects within mass limits suitable for dismounted infantry [7]. Yet, their relatively low muzzle velocities (typically <300 m/s) and shaped-charge reliance restrict engagement range and efficacy against modern composite armors. Meanwhile, point-defense autocannons and close-in weapon systems (CIWS) such as the Phalanx employ kinetic projectiles at extreme firing rates to intercept aerial threats, although they are hampered by ammunition consumption, high mass, and limited adaptability [8].

Anti-air missile platforms, notably the FIM-92 Stinger and similar man-portable air-defense systems (MANPADS), achieve longer ranges and guidance flexibility at the expense of cost and logistical footprint, rendering them suboptimal for saturation countermeasure or drone-swarm defense [9]. Recent C-RAM and counter-UAS developments have explored distributed launcher arrays and advanced target cueing, yet they typically depend on heavy installations and complex power/cooling systems [10].

Against this background, miniature solid rocket projectiles, combining high-density AP/HTPB monopropellant, thermally resilient liners, and modular casing, are emerging as promising candidates for mid-range, rapid-response applications [2, 5].

Key enabling technologies include additive manufacturing of Inconel 718 casings and nozzles for supersonic exhaust containment [6], as well as polymer insulation strategies using PEEK to withstand transient thermal spikes. Integrated multi-tube and variable-barrel launchers further present new opportunities for staggered, multi-vector engagement against maneuvering threats [3,4].

Recent modeling [1, 10] suggests that such projectile systems can achieve penetration profiles comparable to APFSDS rounds (e.g., >100 mm RHA), while maintaining flexible deployment options—dismounted, rooftop, or vehicular, thus offering scalable solutions for both conventional and asymmetric security environments.

1.1. The anti-air defense combined cannons system

The evolving landscape of aerial threats, including unmanned platforms, saturation rocket artillery, and advanced cruise missile systems, necessitates a layered, adaptive approach to national air defense. The motivation for integrating combined cannons within anti-air defense frameworks stems not only from the need for technological versatility but also from a strategic imperative to maximize cost-effectiveness, operational readiness, and flexibility across multiple missions. Pecht et al. [11] highlight the complexities inherent in selecting multi-task R&D projects, using the case of the Israeli missile defense ecosystem to demonstrate how systems capable of engaging diverse targets (from ballistic missiles to tactical aerial incursions) offer significant advantages over single-purpose solutions. Their findings point to the value of platforms that support both air defense and ground interdiction, underpinned by shared technological cores and modular architecture [11]. In the context of combined cannons (Synergy of Projectile and Guided Systems), recent developments in counter-air artillery emphasize the strategic role of enhanced projectile cannons alongside guided interceptors. Hartlage et al. [12] systematically review the design of the Enhanced Counter Air Projectile (ECAP), observing that advances in ramjet propulsion, aerodynamic shaping, and fusing have extended the reach and effectiveness of kinetic interceptors well beyond legacy autocannons. Compared to pure missile-based solutions, combined cannon systems can deliver high-volume, rapid-response fire against swarms or saturating attacks, while supplemented by interceptors that deliver precision engagement of high-value or maneuvering targets. This hybridization increases defense layers, distributes risk, and reduces per-shot costs, a clear benefit observed in systems that mix solid-propellant rockets with variable-barrel launching platforms, as in the discussed manuscript [12]. Moreover, Williams et al. [13] provide a framework for integrating guided interceptors within broader kinetic defense arrays, stressing that conceptual designs must address not only aerodynamic and propulsion efficiency but also system control logic, cueing integration, and cost trade-offs. The anti-air defense combined cannons system, as presented in the manuscript, exemplifies this by deploying a modular family of 20 mm rocket-propelled projectiles via portable, rooftop, and vehicle-mounted cannons; each capable of contributing to variable interception patterns and multi-vector saturation defense. When juxtaposed with dedicated missile systems, such as guided interceptors and enhanced air projectiles, these cannons demonstrate superior adaptability for

short-and mid-range engagements, cost-sensitive layered defense, and infrastructural integration in both static and mobile scenarios [13].

The collective evidence from the selected references positions combined cannon systems as highly complementary to missile-based interceptors. The Israeli missile defense case study underscores the necessity of project management strategies that value versatility and resource optimization. The ECAP's technical advances clarify how projectile-based defenses offer rapid scaling and minimal logistical burden for widespread deployment. Finally, guided interceptor conceptualization shows that the fusion of smart munitions with kinetic cannons maximizes engagement envelope and mission flexibility, especially against threats with unpredictable trajectories or large salvo volumes [11–13].

In practical terms, the manuscript's anti-air defense combined cannons system bridges crucial gaps:

(i) It achieves rapid-fire, high-volume intercept against saturation attacks (as with salvo rockets or drone swarms);
(ii) Modular barrel and platform configurations ensure deployment adaptability, from soldier-carried to fixed turrets;
(iii) Integration with guided interceptors permits selective engagement of high-value or evasive targets, maximizing operational effectiveness and minimizing resource waste over time.

These attributes directly align with the future trajectory of defense R&D explored in recent comparative research, offering scalable, mission-adaptable protection for both conventional and asymmetric threats.

1.2. The defense projectiles cloud

The evolution of advanced projectile and counter-projectile technologies has fundamentally redefined the battlespace, moving from pure interception or destruction of singular threats toward the management and exploitation of entire clouds of debris, fragments, and reactive effects generated by high-speed impacts. Defense architectures and technologists have recognized that the dynamics of these "projectiles clouds", i.e., the dense swarm of fragments and reactive products resulting from projectile/target interactions, constitute a critical aspect of both threat and protection. In modern air and missile defense, and in broader counter-munition and satellite protection, understanding, shaping, or mitigating the effects of these clouds is as crucial as perfecting the projectile or shield itself [14].

Defense projectiles clouds are most often generated at the instant of high- or hypervelocity impact, where relative velocities (often exceeding several km/s in military or orbital circumstances) instantly convert large fractions of kinetic energy into shock, flash, vaporization, and the formation of fine debris. Recent research has deepened understanding of the mechanisms by which projectile and target materials disintegrate, fragment, or react in such collisions. For instance, Önder [15] demonstrates how the impact of projectiles against wavy or structured plates produces characteristic debris clouds, whose density, particle spectrum, and propagation cone

are highly sensitive to plate geometry and material strength.

Önder [15] experimentally characterizes fragmentation and debris cloud formation resulting from hypervelocity impacts on corrugated (wavy) plate geometries. Using high-speed imaging and post-mortem fragment sizing, it is found that plate geometry and material heterogeneity strongly influence the fragment size spectrum and cloud dispersion, and that intentional geometric perturbations (wavy patterns) increase small-particle production and generate denser near-field fragment clouds. These findings underscore that warhead and target geometries control fragment lethality and the spatial distribution of hazardous debris, with clear implications for collateral risk and the design of defensive intercept strategies.

Similarly, the experiments and modeling by Abdulhamid et al. [16, 17] reveal that the material type (e.g., steel, aluminum, or specialized energetic composites) remarkably influences the size distribution and hypervelocity dispersal of projectile-generated clouds, directly affecting the downstream lethality, shielding requirements, and collateral effects. As Xue et al. [18] observe, the transient impact flash and energy transfer at the point of contact further modulate cloud development, with higher energy density yielding finer, more energetic debris capable of exacerbating secondary damage or defeating thin-layered shields.

The progression to advanced energetic materials for both defense and counter-defense roles has resulted in the deliberate engineering of reactive projectiles designed to amplify the destructive potential of their clouds. Zong et al. [19] review the state-of-the-art in Al/PTFE-based reactive materials, highlighting their application in damage maximization: upon hypervelocity impact, these materials not only fragment mechanically, but also undergo rapid exothermic reactions, enhancing both the temperature and overpressure regime inside the cloud and significantly increasing its lethality against equipotential shielding. This deliberate cloud enhancement has strategic implications for both anti-air/ballistic missile defense (BMD) and anti-personnel/area denial realms. Deploying projectiles that create highly damaging, fast-expanding clouds can both increase interception probability and impose additional design burdens on adversary shield technology.

The nature of the target's protection, multilayered, wavy, or composite-plate structures, is no less important than projectile characteristics, as these govern the evolution, spread, and secondary generation of debris clouds. Liu et al. [20] provide an in-depth analysis of Whipple Shield configurations, commonly used in spacecraft for orbital debris protection; their results demonstrate that modifications in shield surface treatment, as well as initial impactor geometry, drastically alter the cloud's spatial development and particle velocity field. These findings, though primarily oriented toward orbit, have direct analogs in terrestrial defense: modular composite/Whipple-style barriers for air defense installations can induce early breakup and "dilution" of incoming threat clouds, reducing their penetrating power. Recognizing the complexity of emergence and destructiveness of projectile clouds, accurate simulation tools have become a cornerstone of system design and threat analysis. Sophisticated orbital debris cloud propagation studies underscore the necessity of high-fidelity modeling to predict the movement, density, and lifespan

of fragment clouds in space [21]. These methodologies have migrated to military simulation environments, enabling the assessment of multi-layered defense efficiency under varying angles, energies, and engagement geometries. The simulation paradigm was extended by Peng et al. [22] to terrestrial impacts and the collateral damage produced by explosive reactive armor and secondary fragmentation, demonstrating the criticality of predicting not just the primary interception or kill effect, but also the behavior and risk profile of neglected cloud fragments and blast products for both attackers and defenders.

The convergence of these engineering, materials, and modeling advances has established the defense projectiles cloud as both an operational threat that must be mitigated and, in some contexts, a tool to be harnessed for layered defense effectiveness. Many of these developments were anticipated [14], highlighting how ballistic missile defense strategies must contend with not only the intentional deployment of cloud-generating sub-munitions (such as MIRVs or decoys), but also the byproducts of successful intercepts, which can create dangerous secondary clouds at high altitudes or in orbital space.

This duality is also reflected in modern fixed and mobile defense concepts, such as the variable-barrel, multi-projectile interceptors described in the referenced manuscript. These platforms may exploit dense, overlapping fragment clouds to maximize the envelope of certain kill or denial, especially against swarming drones or close-flight rockets, while also requiring robust management of own-cloud collateral effects, particularly in complex urban and allied-force environments.

The main parameters of the projectiles cloud are:

(i) Material and Geometry Influence: Advanced projectile compositions (such as Al/PTFE, energetic composite) and tailored shapes (blunt, ogive, or wavy plates) can increase or modulate cloud destructiveness and energy propagation [15,19].
(ii) Shielding Evolution: Multi-layered, composite, and actively cooled shields now factor in not only stopping power against a projectile, but also dispersion, local energy management, and "cloud shaping" [20].
(iii) Simulation and Predictive Fire Control: Modern intercept and anti-air systems leverage real-time modeling of cloud development and debris trajectories, as in the orbital and terrestrial studies by Williams et al. [21] and Peng et al. [22], respectively.
(iv) Operational Integration: Integration of variable-barrel, rapid-fire systems, as illustrated in the subject manuscript, aligns with the approach of maximizing controlled fragment/debris clouds to saturate threat envelopes, multiply hit probability, and deny area access.

Through these modalities, the "projectiles cloud" has evolved into a keystone construct of 21st-century defense, simultaneously a challenge for system survivability and a new avenue for maximizing the defensive footprint of kinetic and energetic countermeasures.

Furthermore, recent investigations into hypervelocity impact fragmentation, short-term debris cloud evolution, and shock-driven reactivity provide important

context for the design choices and application envelopes proposed in this study. Shu et al. [23] extend the analysis of transient debris clouds into a long-range, system-level context by modeling short-term cloud evolution in the near-field of high-energy collisions (here applied to orbital collision scenarios). Their work emphasizes the role of initial fragment velocity distribution, aerodynamic deceleration, and local flow conditions in defining the temporal and spatial evolution of fragment clouds. Critically, Shu et al. quantify how quickly a dense near-field cloud disperses and how that dispersion depends on initial kinetic spectra and background medium characteristics. Although the geostationary-orbit context differs from atmospheric engagement, the physical principles (fragment momentum distribution, aerodynamic coupling, and temporal dilution) are directly translatable to assessments of collateral hazard in atmospheric intercepts and to the design of "projectiles-cloud" defensive modes.

Tian et al. [24] document a phenomenon that is orthogonal yet practically consequential: shock-driven reaction in energetic PTFE/Al composites can produce short-term pressure perturbations and localized energy release under shock compression. Their experimental campaign demonstrates that reactive constituents can amplify peak pressures and produce late-time energy release beyond what would be expected from inert material deformation alone. The study thereby establishes a cautionary design trade-space: incorporation of reactive materials can markedly increase terminal effect per unit mass, yet at the expense of added environmental, safety, and handling complexity.

Relative to these works, the present 20 mm SRM projectile and launcher suite occupy a distinct portion of the design space with several practical advantages. First, the proposed concept emphasizes a high-sectional-density, kinetic-penetrator approach (tungsten-alloy ogive, $\rho \approx 19$ g/cm³) coupled with a compact SRM that achieves ≈1400 m/s muzzle velocity and analytically predicted RHA-equivalent penetration on the order of 116 mm (≈140 mm into representative composite laminates). Compared with Önder's [15] fragmentation-focused experiments, the projectile is deliberately designed to minimize large-scale fragment production at terminal interaction by favoring mass-concentrated penetration rather than distributed fragmentation; this reduces the creation of dense near-field debris clouds documented by Önder [15] and, as such, limits collateral hazard in urban operational environments. Second, Shu et al.'s [23] quantitative descriptions of near-field cloud dilution validate the operational rationale of the system's "defensive cloud" mode: rather than relying on a single energetic fragmentation event, distributed launches from multiple platforms and pre-biased barriers exploit the rapid geometric dilution described by Shu et al. [23] to create a high-probability intercept volume while maintaining lower per-round collateral signature. In practice, this approach uses kinetic interceptors fired in coordinated time-phased salvos to form a transient volumetric barrier that reduces the need for deliberately fragmenting warheads and mitigates persistent debris hazards. Third, Tian et al. [24] demonstrate that embedding reactive materials can materially alter pressure and thermal signatures at impact. The present design intentionally treats reactive inserts as a secondary option: while reactive fillers (e.g., Al/PTFE combinations) could increase post-impact energy deposition, the manuscript emphasizes the trade-offs,

particularly, environmental emissions, handling and storage complexity, and stricter regulatory burdens identified by Tian et al. [24]. As a result, the baseline design retains an inert kinetic penetrator with modular provisions for controlled energetic layers only in specialized variants subject to rigorous safety and environmental mitigation protocols. This conservative posture preserves the logistical simplicity and safety of the common 20 mm round across multiple launcher platforms while leaving an engineering path open for future, highly-controlled reactive variants.

Finally, the proposed design incorporates manufacturing and thermal-management advantages not addressed in the cited studies. Selective Laser Melting (SLM) of Inconel 718 enables integrated nozzle/casing geometries and robust thin-wall structures that achieve favorable hoop-stress margins under the short, high-heat pulses of the SRM; the PEEK liner combined with a phenolic ablative nose provides a thermal architecture that confines heat flux to sub-millimeter boundary layers and limits liner mass loss during the 2.5 s burn (as shown analytically herein). These features allow the projectile to achieve high exit velocities and consistent ballistic performance while minimizing undesired fragment production and environmental effluent, advantages that complement and address concerns raised by Önder [15] and Verrar et al. [25].

In summary, the three recent studies collectively illuminate the physical mechanisms (fragment production, cloud dispersion, and reactive amplification) that determine terminal effects and collateral risk. The present design differentiates itself by deliberately trading fragment-generating terminal mechanisms for concentrated kinetic penetration, by using coordinated distributed firing to produce controlled intercept volumes rather than single-event fragment clouds, and by maintaining a conservative stance on reactive materials to preserve safety and environmental compatibility. These choices are informed both by the empirical insights of the cited works and by the analytical and experimental validation program proposed in this manuscript.

The design of modern kinetic interceptors must account for the complex dynamics of projectile-target interaction. Recent research (2024–2025) has shifted focus from singular interception to the management of "projectile clouds" - the swarm of debris and reactive effects generated by high-speed impacts. Önder [15] recently demonstrated that target geometry and material heterogeneity strongly influence fragment cloud dispersion, while Shu et al. [23] quantified the rapid aerodynamic dilution of these clouds in near-field engagements. Furthermore, Tian et al. [24] highlighted that while reactive material inclusions (e.g., PTFE/Al) can amplify lethality, they introduce significant collateral and environmental complexities.

Unlike systems that rely on indiscriminate fragmentation, the proposed 20 mm projectile prioritizes high-sectional-density kinetic penetration. By utilizing a tungsten-alloy ogive and minimizing explosive fillers, the design mitigates the risks of uncontrolled debris clouds in urban environments, addressing the collateral concerns raised by Önder [15] and Shu et al. [23], while maintaining the option for "volumetric denial" through coordinated, multi-barrel salvo firing described later in this work.

Moreover, Abdulhamid et al. and Xue et al. [16–18] investigate penetration, fragmentation, and impact-flash phenomena for high-velocity projectiles and show that material selection and impact geometry strongly affect cloud formation and

residual lethality. Zong et al. [19] review Al/PTFE reactive materials that greatly enhance post-impact thermal/pressure effects and are relevant where energetic clouds are desired. Liu et al. [20] and Williams et al. [22], respectively, document advanced simulation frameworks for fragment cloud propagation and C-RAM effects.

Within this technological context, the present study introduces a 20 mm rocket-propelled projectile system comprising AP/HTPB monopropellant, Inconel 718 structural elements, and PEEK thermal insulation. The present manuscript uses the aforementioned recent findings to inform ablation, penetration, and cloud-propagation assumptions and to place our device in the landscape of contemporary research [20–24].

Building on this foundation, and continuing the studies of Tian et al. [24], Verrar et al. [25] and Levitan et al. [26] on solid propellant motor and ramjet projectile, respectively, the current manuscript investigates and validates the integrated design and operational potential of a 20 mm rocket-propelled projectile platform, focusing on:

(i) Ballistic modeling and optimization of grain geometry, chamber flow, and nozzle expansion for sustained Mach 4 performance;
(ii) Thermal protection and structural resilience during firing and flight;
(iii) Comparative penetration, range, and rate-of-fire analysis vis-à-vis legacy systems;
(iv) Modular launcher deployment spanning soldier-portable, rooftop, and vehicle/ship integration;
(v) Scalable defense adaptability for emerging threats, including drones, loitering munitions, and light armor.

This study contributes a quantitative, multi-platform framework for next-generation point-defense systems, aiming to reduce logistical burden, elevate intercept flexibility, and expand tactical response capabilities.

2. Propulsion system design

Grain geometry and motor performance

The propulsion system utilizes approximately 0.127 kg of an ammonium perchlorate/hydroxyl-terminated polybutadiene (AP/HTPB) composite propellant, configured in a cylindrical grain geometry. The grain consists of three segments, each with an outer diameter of 24 mm, an inner port diameter of 12 mm, and a length of 50 mm. This configuration delivers a total impulse of 300 Ns over a burn duration of 2.5 s. The system operates at a chamber pressure of 8 MPa, with a throat diameter of 4 mm, an expansion ratio of 5:1, and an exit diameter of 9 mm, producing an exit Mach number and corresponding exit pressure indicative of under-expanded flow at sea level ambient pressure (0.10 MPa). The relationship between grain geometry, chamber pressure, exhaust velocity, and total impulse is analyzed in this section (**Figure 1**).

Chamber pressure as a function of grain geometry is defined by:

$$p_c = k\left(\frac{b_g}{A_t}\right)^n \tag{1}$$

where b_g is the grain burning surface [m^2], A_t—throat area [m^2], k—initial pressure

value and n pressure exponent (power-law index).

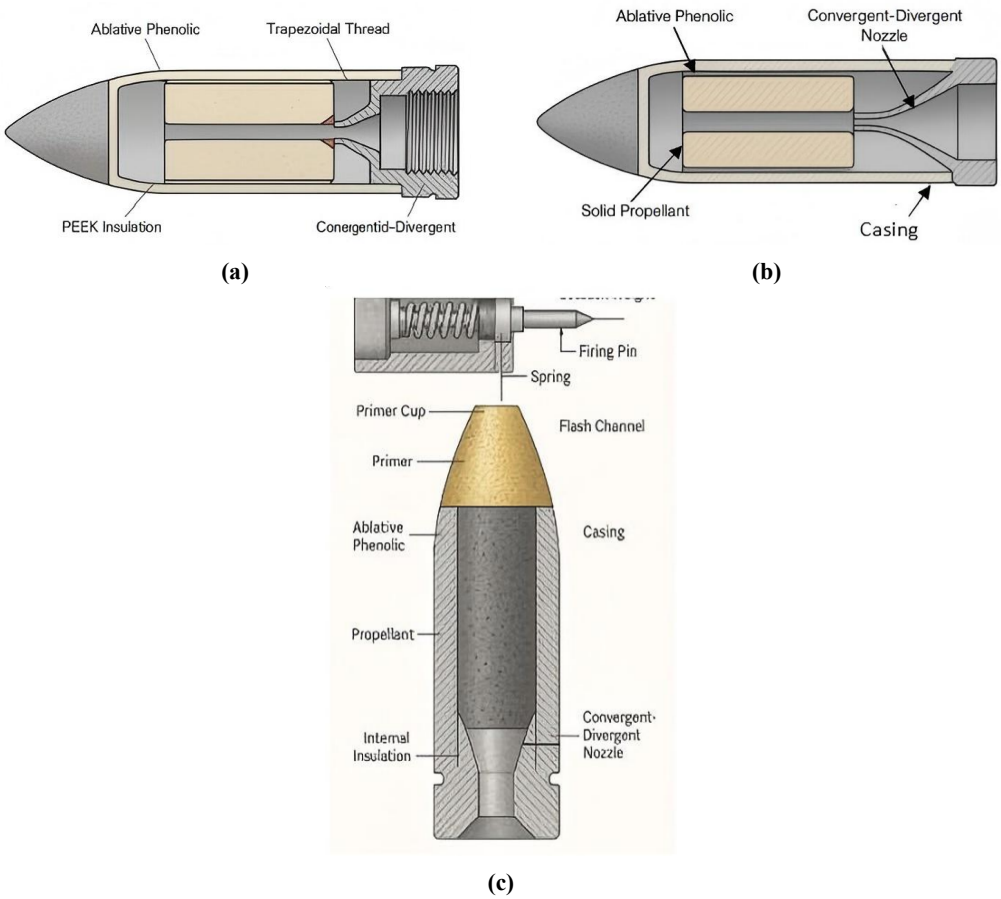

Figure 1. Projectile Assembly: **(a)** Assembled configuration with threaded adapter for experimental mounting or integration with an alternative launch device; **(b)** Optimized projectile design excluding the threaded assembly; **(c)** Complete projectile with integrated ignition system.

For isentropic nozzle, the area ratio is given by:

$$\frac{A_e}{A_t} = \left(\frac{T_0}{T_e}\right)^{\frac{\gamma+1}{2(\gamma-1)}} \tag{2}$$

where $A_e[m^2]$ is the nozzle exit area section, $T_0\ [K],\ T_e\ [K]$ represent the stagnation point and nozzle exit temperatures, and γ constant is the specific heat ratio parameter, respectively.

The target thrust (F) is determined by:

$$F = \dot{m} u_e \tag{3}$$

where the parameters $\dot{m}$, u_e represent mass flow and gas exit velocity, respectively.

The appropriate total impulse (I) after burning time (t_b) is:

$$I = F \cdot t_b, \quad t_b \leq 3\ s \tag{4}$$

Throat area, from known chamber pressure (p_c), thrust (F) and thrust coefficient (C_F), is calculated as:

$$A_t = \frac{F}{C_F \cdot p_c} \tag{5}$$

Exit area:

$$A_e = \epsilon \cdot A_t \tag{6}$$

The area extension (divergence) ratio is denoted by ϵ. Required propellant mass:

$$m_p = \frac{I_{total}}{I_{sp} \cdot g_0} \tag{7}$$

Grain Geometry and Burn Rate are calculated, by assuming cylindrical grain burning (r_b) from internal surface (neutral burn) as:

$$r_b = a \cdot p_c^n \tag{8}$$

where *a* and *n* are empirical coefficients.

Volume of propellant (V_p) required is calculated through the propellant mass (m_p) and its density (ρ):

$$V_p = \frac{m_p}{\rho} \tag{9}$$

Grain design volume (V) is therefore:

$$V = \pi \cdot L \cdot \left(r_o^2 - r_i^2\right) \tag{10}$$

where its length, external and internal diameters are denoted by L, r_o, r_i, respectively.

Hence the total volume V_{total} is determined using number of grain segments (n) multiplied by (10):

$$V_{total} = n \cdot V \tag{11}$$

3. Thermal and structural analyses

Using the thin-wall approximation, the hoop stress (σ_θ) through wall thickness (t) under internal combustion pressure (p_c) is given by:

$$\sigma_\theta = \frac{p_c \cdot r_i}{t} \tag{12}$$

A safety factor (S.F.) against yield strength (σ_{yield}) from (12) at elevated temperature is:

$$\text{S.F.} = \sigma_{yield}/\sigma_\theta \tag{13}$$

A thermal gradient of approximately $\Delta T \approx 2600K$ generates transient thermal stresses that remain below the material's high-temperature yield strength due to the brief exposure duration during burn:

$$\sigma_T = E \cdot \alpha \cdot \Delta T \tag{14}$$

Peak stress at the Nozzle throat (with diameter r_t) is expressed as:

$$\sigma_{\theta,throat} = \frac{p \cdot r_t}{t} \ll \sigma_{yield} \tag{15}$$

To evaluate *boundary-layer* development at the throat, the supersonic boundary layer thickness (δ) is estimated by:

$$\delta = \sqrt{\frac{2x}{Re_x}} \tag{16}$$

Where Reynolds number is defined by $Re_x = \rho_e u_e x/\mu_e$. The characteristic length, gas density and gas dynamic viscosity at the nozzle exit are defined by the symbols x, ρ_e, μ_e. At the throat Reynolds number (Re_t) fulfills together with the appropriate throat parameters:

$$Re_t = \rho_t u_t D_t/\mu_t \tag{17}$$

For a turbulent boundary layer over a characteristic distance x:

$$\delta \approx 0.37 x Re_x^{-1/5} \tag{18}$$

This results in a very thin boundary layer, ensuring that solid particles (≥1 μm) remain entrained within the core flow and do not adhere to the nozzle wall. At high Mach numbers, detached bow shocks in front of blunt projectiles stand off by several millimeters, effectively mitigating peak thermal and pressure loads on the nose cone. Aerothermal heating during flight induces a recovery (stagnation) temperature at the nose tip:

$$T_0 = T_\infty \left(1 + \frac{\gamma - 1}{2} M^2\right) \tag{19}$$

The nose tip experiences the highest heat flux, and the use of ablative thermal protection systems (e.g., carbon-phenolic) is essential, as they are rated for temperatures exceeding 2000 ℃, providing protection through slow ablation and endothermic decomposition.

4. Ablation and erosion

The convective heat flux to the nozzle wall is estimated using the Bartz correlation:

$$\dot{q}_w = \frac{0.026}{D_t^{0.2}} \cdot \left(\frac{\mu^{0.2} \cdot c_p \cdot {P_r}^{0.6}}{A_t^{0.2}}\right) \cdot \frac{p_c^{0.8}}{T_0^{0.6}} \cdot \left(1 + \frac{r_c}{D_t}\right)^{-0.1} \tag{20}$$

where μ, c_p, $\dot{q}_w$, p_c, r_c, D_t, T_0 are the dynamic viscosity [kg/m · s], specific heat [J/kg · K], wall heat flux [W/m^2], chamber pressure [Pa], chamber radius [mm], throat diameter [mm] and stagnation combustion gas temperature [K], respectively. The convection heat flux ($\dot{q}_{conv}$) is assumed approximately equal to the total convective heat input $\dot{q}_{conv} \approx \dot{q}_w$.

Using the semi-infinite solid approximation, the wall temperature rise due to heat conduction is:

$$\Delta T = \frac{\dot{q}_w \cdot \sqrt{t_b}}{\sqrt{\pi \cdot \rho \cdot c_k \cdot k}} \tag{21}$$

where k is the conductivity coefficient. The radiative heat flux to the wall ($\dot{q}_{rad}$) is given by:

$$\dot{q}_{rad} = \varepsilon_{wall} \cdot \sigma \cdot F_g \cdot \left(T_g^4 - T_w^4\right) \tag{22}$$

where ε_{wall}, σ, F_g, T_g, T_w are the wall emissivity, Stefan-Boltzmann constant ($5.67 \times 10^{-8}\mathrm{W/m^2 \cdot K^4}$), configuration view factor ($\approx$1 for throat cavity), gas temperature $\approx$ 3000 K, and wall temperature $\approx$ 700 K (acceptable Inconel backend temp), respectively. The total heat flux at the throat is the sum of convection and radiation components:

$$\dot{q}_{total} = \dot{q}_{conv} + \dot{q}_{rad} \tag{23}$$

To provide a conservative design estimate, the required wall thickness using a 1D slab conduction model is:

$$\dot{q}_{total} = \frac{k \cdot \Delta T}{t} \rightarrow t = \frac{k \cdot \Delta T}{\dot{q}_{total}} \tag{24}$$

Alternatively, the Nagler model [27] provides the convective heat transfer coefficient as:

$$h_c = \frac{q_{convection}}{T_s - T_i} = \frac{q_{convection}}{\Delta T} \tag{25}$$

where the convective heating flux rate $q_{convection} = h_c\left(T_s - T_i\right) \approx 4.2[\mathrm{MW/m^2}]$ [27]. $T_i, T_{char}, T_s (T_{char} < T_s)$ are the ambient environment temperature, temperature at onset of surface charring, and surface exposed temperature of the char layer. The appropriate total erosion depth due to surface charring is:

$$x_s = u_s t_s = \frac{q_{convection}}{\rho_s C_p\left(T_s - T_{char}\right)} t_b \tag{26}$$

where t_b is the total exposure burn time, ρ_s, V_s are protective shield ablative material specimen density and volume, respectively. C_p is the specific heat capacity of ablative material.

The total erosion due to both convection and radiation ($u_{convection\ \&\ radiation}$) is:

$$x_{convection\ \&\ radiation} = u_{convection\ \&\ radiation} t_s = \left[\frac{q_{convection}}{\rho_s C_p\left(T_s - T_{char}\right)} + \frac{q_{radiation}}{\rho_s C_p\left(T_s - T_{char}\right)}\right] t_s \tag{27}$$

Where $q_{radiation} = \varepsilon_{wall}\sigma F_{1\to 2}\left(T_s^4 - T_i^4\right) \approx 4.6[\mathrm{MW/m^2}]$. The parameters $\sigma = 5.67 \cdot 10^{-8}[\mathrm{W/(m^2K^4)}]$, $F_{1\to 2} = 1$ are the Stefan-Boltzmann constant, view factor (assuming from one surface to another only-throat cavity) and wall emissivity ($\varepsilon_{wall} \approx 1$), respectively. The typical values based on Nagler [27] (see there the empirical references) are $\mathrm{T_s} = 3000$ ℃, $\mathrm{T_i} = 25$ ℃, $\mathrm{h_s} = 1417\left[\frac{\mathrm{W}}{\mathrm{m^2K}}\right]$. In case of PEEK heat protective insulation shield parameters based on Patel et al. [28] are

T_{char} = 650 ℃, ρ_s = 1320 $\left[\frac{\text{kg}}{\text{m}^3}\right]$, C_p = 1340 $\left[\frac{\text{J}}{\text{kgK}}\right]$, the obtained values for the erosion rate and distance are u_s = 1.01 mm/sec and x_s = 2.53 mm for total burning time of 2.5 s. In the case of radiation and convection the appropriate contribution radiation term to the erosion rate and total erosion rate will be $u_{radiation}$ = 1.11 mm/sec and $u_{radiation\ \&\ convection}$ = 2.14 mm/sec, $x_{convection\ \&\ radiation}$ = 5.35 mm.

4.1. Insulation and thermal design of projectile

The aerodynamic (ram) heating during atmospheric flight is given by:

$$q_{ram} = C_h \rho D v^3 \tag{28}$$

where $C_h \approx 1.2 \times 10^{-9}$, ρ_{gas} = 1.2 kg/m^3, D = 0.02. Assuming 30% ablation efficiency (η = 0.3), and using the specific enthalpy of ablation L_{abl} [J/kg], the mass loss rate due to ablation is:

$$\dot{m}''_{\text{abl}} = \eta \frac{\dot{q}_{total}}{L_{\text{abl}}} \tag{29}$$

Over the total t_b burn duration, the liner thickness loss is:

$$\Delta t = \frac{\dot{m}''_{\text{abl}}}{\rho_{\text{PEEK}}} t_b \tag{30}$$

4.2. Particle entrainment vs. mass flow

The total mass of ablated particles from the nozzle is estimated as:

$$m_{abl,\ total} \approx \dot{m}''_{\text{abl}} A_{wet} t_b \tag{31}$$

where the nozzle wetted area is approximated by $A_{wet} \approx \pi\,(\mathrm{D_t} + \mathrm{D_e})\,/2 \times \mathrm{L_{Nozzle}}$.

The total gas mass flow is:

$$m_{gas,\ total} = \dot{m}_{gas} t_b \tag{32}$$

The ratio of particle mass to gas mass should remain:

$$\frac{m_{abl,\ total}}{m_{gas,\ total}} < 2\% \tag{33}$$

This represents minimal particle loading: the entrained solid particles (typically micron-sized) are easily transported by the core gas flow without risk of nozzle choking or agglomeration.

5. Aerodynamics

For an ideal (isentropic) gas with ratio of specific heats γ, the Mach number M_e at the exit of a diverging nozzle of area ratio:

$$\frac{A_e}{A^*} = \frac{A_e}{A_t} \tag{34}$$

satisfies the implicit "area–Mach" relation:

$$\frac{A_e}{A^*} = \frac{1}{M_e}\left[\frac{2}{\gamma+1}\left(1+\frac{\gamma-1}{2}M_e^2\right)\right]^{\frac{\gamma+1}{2(\gamma-1)}} \tag{35}$$

From isentropic relations the static-exit pressure is:

$$\frac{p_e}{p_0} = \left(1+\frac{\gamma-1}{2}M_e^2\right)^{\frac{\gamma}{1-\gamma}} \tag{36}$$

If $p_e > p_a$ (ambient pressure), the flow is under-expanded, and no internal shocks occur within the nozzle. The jet continues to expand after exiting, forming expansion fans rather than requiring normal or oblique shock waves for pressure adjustment. To prevent shock-induced flow separation, the nozzle should be designed with (i) a small divergence angle, and (ii) smooth curvature to maintain supersonic boundary layer attachment. This approach ensures efficient supersonic flow expansion without internal instability or performance losses.

6. Impact and penetration capability

Hydrodynamic penetration model

For high-velocity rigid penetrators impacting rolled homogeneous armor (RHA), the idealized hydrodynamic penetration depth (P_{RHA}) is approximated by:

$$P_{RHA} = L_n\frac{\rho_p}{\rho_t} \tag{37}$$

where L_n, ρ_p, ρ_t represent the length of the penetrator, density of the penetrator and density of the target, respectively. With the appropriate dynamic impact stress approximation:

$$\sigma_{impact} \approx \sqrt{E\rho u^2}, \quad KE = \frac{1}{2}\rho u^2 \tag{38}$$

where E, u, ρ are the Young's modulus, impact velocity and penetrator density, respectively.

Empirical evidence suggests penetration increases with velocity. A correction factor based on impact velocity is introduced $(u/1000)^{0.5}$:

$$P_{RHA,\,correction} = L_n\frac{\rho_p}{\rho_t} \times \sqrt{\frac{u}{1000}} \tag{39}$$

Against modern composite laminates, penetration effectiveness is typically enhanced. A conservative correction factor of 1.2× is applied for composite armor:

$$P_{COMP} \approx 1.2 \times P_{RHA,\,correction} \tag{40}$$

This is representative of the increased performance of modern ceramic-steel-fiber laminates, which often provide enhanced resistance while remaining lightweight.

7. Ignition mechanism

The ignition system shown in **Figure 1** is a fully self-contained, mechanically armed, pyrotechnic device, activated autonomously upon projectile barrel exit. No external igniter is required. The system is embedded within the projectile base and incorporates multiple integrated safety features.

A mechanically-armed, setback-driven firing pin strikes a percussion primer upon barrel exit, initiating a flash-to-main transfer via a black-powder channel. Spin-safe arming and shear-ring features ensure safety under handling. Below is a fully self-contained, mechanically-armed, pyrotechnic "bullet-exit" igniter that requires no external igniter device; everything is built into the projectile base and fires automatically as it leaves the barrel.

The mechanism overview in **Figure 1** includes:

(i) *Setback-Armed Firing Pin:* A small inertial mass ("setback weight") compresses a spring-loaded firing pin upon acceleration > 10,000 m/s². This overcomes the spring preload, driving the pin into the primer.

(ii) *Percussion Primer Cup:* A compact primer (e.g., lead styphnate-based, similar to a 209-shotgun primer) housed in a metal cup is struck by the firing pin, producing a flash and high-pressure gas.

(iii) *Flash-to-Main Transfer Train:* The flash is channeled through a black powder or Ti/$KClO_4$-based pyrotechnic column (Ø1 mm, ~5 mm long), providing time-delay and thermal energy transfer to the main grain. This bridges into the main propellant port and ignites the AP/HTPB grain.

(iv) *Spin-Safe Arming:* A threaded shear ring prevents pin movement until the projectile completes ~10 rotations, ensuring arming occurs only after sufficient rifling-induced spin, thus preventing unintentional ignition.

7.1. Setback force activation

The projectile is ignited by a setback-armed mechanical primer system. The setback force (F) is generated by acceleration a acting on a small mass m_w:

$$F = m_w \cdot a \tag{41}$$

Let m_w = 0.03 grams (setback weight), spring preload F_s = 10 N, then the minimum required acceleration:a = 3,4000 g; Such acceleration is easily reached during muzzle exit.

7.2. Primer energy delivery

The spring stores potential energy E when compressed by distance x:

$$E = \frac{1}{2}kx^2 \tag{42}$$

With k = 1000 N/m, x = 1 mm, E = 0.0005 J. Multiple spring coils or increased compression stroke can raise energy levels above 1 J, threshold sufficient for reliable primer ignition.

7.3. Flash channel delay

Delay time for the black powder flash channel train of length L and burn rate r_b is:

$$t_d = \frac{L}{r_b} = 5\ ms \tag{43}$$

for L = 5 mm and burn rate r_b = 1 mm/ms. This delay ensures ignition (flame delivery synchronization) occurs only after full projectile clearance from the launcher.

8. Launcher configuration—dynamic response models

8.1. Shoulder-fired launcher recoil

The recoil impulse (I) due to projectile ejection is:

$$I = m_p \cdot u \tag{44}$$

The recoil velocity of the launcher with mass M is:

$$u_r = I/M \tag{45}$$

where m_p = 0.18 kg, M = 2.5 kg and u = 1400 m/s then I = 252 N · s and u_r = 100.8 m/s, respectively. This is mitigated through recoil-dampening mechanisms such as a shoulder rest or compensating spring system.

8.2. Fixed interceptor rate and targeting firing rate

For a launcher pod with N tubes and a cycle time t_c:

$$R = \frac{N}{t_c} \cdot 60 \tag{46}$$

For instance, in case of N = 12, t_c = 1.2 s, then, R = 600 rounds/min.

Turret angular response (second-order step response):

$$\theta(t) = \theta_{cmd}(1 - e^{-\zeta\omega nt}) \tag{47}$$

where damping ration ζ = 0.7, the natural frequency ω_n = 30 rad/s. To reach $\geq$ 90% of the commanded angle θ_{cmd}, the response time solution is $\theta(t) \geq 0.9\ \theta_{cmd} \Rightarrow t \approx$ 0.1–0.15 s. This enables rapid sequential retargeting of multiple threats.

Accordingly the *Functional Sequence* will be composed from the following steps:

(i) *Launch & Setback* (0→0.5 ms): Muzzle exit acceleration (~15,000 g) drives setback weight forward. After ~0.5 ms, pin overcomes (compresses) spring and strikes primer.

(ii) *Primer Ignition* (0.5→1 ms): Primer detonates by firing pin strike, generating ~ 20 MPa (200 bar) peak pressure in cup, igniting flash in the channel.

(iii) *Flash Train Burn* (1→6 ms): Delay mix in channel such as pyrotechnic composition propagates flame through the channel.

(iv) *Main Grain Ignition* (≈6 ms): Flash reaches propellant port grain, ignites

AP/HTPB grain, chamber pressure rises to ~8 MPa and burn sustains for ~2.5 s.

The appropriate safety & reliability requirements are:

(i) *Spin-Safe Shear Ring*—Aluminum shear ring engages setback weight. Requires ~20 N·mm torque (from ~500 Hz rifling spin) to disengage, preventing premature ignition (to unscrew before pin can move).

(ii) *Spring Preload Safety Margin*—Preload tuned to resist accelerations <5000 g, ensuring drop and handling safety.

(iii) *Primer Isolation Seal*—An O-ring seals the primer cup, preventing gas blowback and unintended ignition paths.

Integration into the small base diameter (~Ø20 mm) requires overall base length of 10 mm; *Internal Machining*: Thread-free to allow clear flash passage, internal smooth bore connects channel to combustion chamber; *Material*: Body should be made of Inconel 718 additively manufactured, and primer cup should have Brass insert.

This design ensures high thermal resistance, mechanical integrity, and self-contained functionality for compact high-performance projectiles.

9. Results and discussion

9.1. Grain geometry and motor performance

To reach $M_e \approx 4$ the exit velocity should be $u_e \approx 1324$ m/s. For minimum bore diameter D = 20 mm, the performance values based on Equations (1)–(4) are presented in **Table 1**. It was chosen $L = 50$ mm to ensure ≥ M4.

Table 1. Grain length versus performance parameters.

Grain length L (mm)	P_c[MPa]	$\dot{m}$ (g/s)	Predict. u_e (m/s)
40	6.5	1.8	1300
50	8.2	2.4	1400

9.2. Casing and nozzle materials

The motor casing and nozzle are fabricated from Inconel 718 via SLM, with a 1 mm wall thickness. A PEEK thermal liner (5.35 mm at the throat, 0.8 mm elsewhere) provides insulation against an estimated total heat flux (convection + radiation) of up to 8.8 MW/m².

9.3. Combustion pressure and hoop stress

Using a thin-wall approximation, the hoop stress in the Inconel shell under 8 MPa internal pressure is 96 MPa, yielding a safety factor of 8.6 against the material yield strength at high temperature (830 MPa) (see Section 1). Linear thermal expansion across $\Delta T \approx 2600$ K induces a stress of 609 MPa, which remains below the high-temperature yield of Inconel 718, given the short exposure time of the burn.

9.4. Boundary-layer thickness

Applying the rotating-cone model [29], the supersonic boundary layer at the throat ($Re_x \approx 5 \times 10^5$, x = 10 mm) has thickness: $\delta \approx 0.2$ mm. Even at Mach 4 and colder ambient conditions, it remains well below 1 mm, substantially less than the 0.8–1.5 mm PEEK insulation thickness. This ensures the boundary layer confines the heat flux near the surface and supports flow attachment along the 15° divergent contour [30]. The turbulent boundary-layer thickness over x ≈ 10 mm is roughly $\delta \sim 0.37 \times Re_x^{-1/5}$. A very thin layer: particles (≥1 μm) remain entrained in the core, not in the wall film. Milman [30] shows that detached bow shocks for blunt bodies at Mach 4 stand off by several millimeters, mitigating peak thermal and pressure loads on the projectile nose. Aerothermal Heating During Flight: At Mach 4, total recovery temperature (from stagnation): Nose tip experiences peak heat flux. Ablative phenolic (e.g., carbon-phenolic) rated to >2000 °C. Effective with slow ablation and heat absorption.

9.5. Ablation and erosion

In case of unrealistically thin thickness due to the assumption of perfect conduction, one should add safety factor of 10–20× to account for: Ablation, Imperfect contact, Thermal spiking. It may also been bonded or mechanically fixed, by extending the PEEK liner inside the nozzle section or co-mold with an ablative layer such as silica phenolic. An analytic demonstration that any ablation (solid particle or pyrolysis gas) in convergent–divergent nozzle during the ≈2.5 s burn will be both too small to compromise the flow and too slow to damage the structural liner is presented.

9.6. Insulation and thermal design of projectile

Total heat flux at throat ≈ 8.3 MW/m² (convection and radiation). PEEK thickness ~1.5 mm. Add *graphite-phenolic ablative nose*, thickness ~2 mm, to limit skin heating during flight. Estimate flight heating: $q_{ram} = C_h \rho D v^3 \approx 1.2 \times 10^{-9} \times 1.2 \times 0.02 \times 1372^3 = 0.76\ MW/m^2$. Where $C_h \approx 1.2 \times 10^{-9}$, $\rho_{gas} = 1.2\ kg/m^3$, D = 0.02. Accordingly, nominal; PEEK attached to phenolic material is adequate. Assuming a 30% ablation efficiency of the total heat flux, the resulting mass loss rate is: $\dot{m}''_{abl} = \frac{0.3 \cdot 8.3 \times 10^6}{2.0 \times 10^6} \approx 1.25\ kg/m^2 \cdot s$. Over a 2.5 s burn, the worst-case liner loss becomes: $\Delta t = \frac{\dot{m}''_{abl}}{\rho_{PEEK}} t_b = \frac{1.25}{1320} \times 2.5 \approx 2.4$ mm. The remaining 1 mm—thick Inconel shell preserves full mechanical strength. With total ablation products <1.3% of exhaust mass, the flow remains unchoked and unobstructed.

9.7. Contour flow attachment and divergence angle to prevent separation

Even in an under-expanded nozzle the boundary-layer separation might be a challenge to overcome if the wall-angle is too steep. Current design uses:

(i) *Convergent half-angle* = 45° over 5 mm (very short; purely to choke).

(ii) *Divergent half-angle* = 15° over 15 mm (a "bell-style" or gently expanding cone). A 15° half-angle is below the typical 17°~20° threshold ($\theta_{diverge} = 15^\circ < 17^\circ \sim 20^\circ$) for incipient separation in supersonic nozzles, and the

smooth radius at the throat–divergence junction ("Rao-style" curvature contour or similar) ensures that the Mach 2.5 core sees a continuous pressure gradient that keeps the boundary layer attached and follows the rigid walls without separation or shock formation, preventing any low-pressure recirculation pockets where particles might settle. High shear at the wall promises continuously sweep out any ablated debris.

(iii) *Under expanded condition*: $P_e/P_a > 1$ensures that all pressure adjustment occurs in the free jet, not inside. Together, these analytic facts guarantee a shock-free internal flow.

10. Impact and penetration capability

Assuming a tungsten-alloy rigid penetrator nose ($\rho_p = 19\ g/cm^3$) at 1400 m/s ($L_n = 0.04$ m – nozzle length, $\rho_{tungsten} = 7.8\ g/cm^3$) we get using the hydrodynamic penetration model Equation (38) that $P_{RHA} = L_n \frac{\rho_p}{\rho_t} = 0.04 \times \frac{19}{7.8} \approx 98$ mm and appropriate correction for velocity scaling to approximately $P_{RHA,\ correction} = L_n \frac{\rho_p}{\rho_t} \times \sqrt{\frac{1400}{1000}} \approx 116$ mm, respectively. In case of composite target, using 1.2 factor in Equation (39), yields $P_{COMP} \approx 1.2 \times P_{RHA,\ correction} \approx 140$ mm. With a 20 mm-diameter, 175 mm-long rocket-projectile reaching $\sim$ 1400 m/s, a tungsten-alloy nose, and the optimized motor/gas-dynamic design above, one can expect on the order of 115–120 mm RHA penetration and $\sim$ 140 mm into typical modern composite laminates, more than sufficient to defeat light to medium armor and breaching exterior shells as elaborated in **Table 2**.

Table 2. Recommended Target Thicknesses.

Target type	Typical protection level	Expected penetration
Light steel armor	8–12 mm RHA equivalent	116 mm
Medium steel armor	20–50 mm RHA	Partial (>50 mm)
Composite vehicle armor	60–80 mm ceramic-steel laminate	140 mm
Exterior envelopes	5–10 mm mild steel shell, composite panels	Full breach

A completely self-contained, bullet-exit-armed igniter that eliminates external igniter hardware and automatically lights the solid grain within ≈ 6 ms of barrel exit; ideal for a compact, handheld M ≈ 4 projectile as elaborated in **Table 3**. Accordingly, the whole projectile's components geometry appear in **Table 4**.

Table 3. Detailed Pyro-Train & Geometry.

Stage	Component	Geometry/mass
Setback Weight	Steel cylinder	Ø2 mm × 3 mm, mass ≈ 0.03 g
Firing Pin & Spring	Inconel pin, 1 mm tip	Spring stiffness: 15 N/mm, pre-load 10 N Travel: 1 mm → 15 N causes movement
Primer Cup	Brass cup, Ø4 mm × 2 mm	Primer mass ≈ 0.2 g (lead-styphnate mix)
Flash Channel	Drill-through SLM nozzle base	Ø1 mm × L5 mm; lined with flash mix (~0.03 g)
Delay/Driving Composition	Black powder flour	Ø1 mm core in channel, burn time ≈ 5 ms

Table 4. Detailed Projectile Components Geometry.

Component	Parameter	Value
Projectile Nose	Shape	Tangent-ogive (k = 5)
	Length L_n	40 mm
	Base diameter	20 mm
	Tip radius	0.2 mm
	Ablative phenolic liner thickness	2 mm
Propellant Grain	Outer diameter D_g	24 mm (casing I.D. + insulation)
	Inner port diameter	12 mm
	Grain length L_g	50 mm
	Port shape	Single cylindrical
	Port surface area per grain	$\pi \cdot D_{port} \cdot L_g \approx 1885$ mm
	Number of grain segments	3 × 16 mm lengths (stacked)
Insulation & Casing	PEEK liner thickness (throat)	5.35 mm
	PEEK liner thickness (conv/div)	0.8 mm
	Casing inner diameter	24 mm
	Casing wall thickness	1.0 mm (Inconel 718 SLM)
	Total casing length	100 mm
Convergent-Divergent Nozzle	Throat diameter D_t	4.0 mm
	Convergent half-angle	45°
	Contraction length	5 mm
	Divergent half-angle	15°
	Exit diameter D_e	9.0 mm
	Expansion length	15 mm
	Nozzle overall length	25 mm
Igniter Adapter	(No thread)	Smooth bore + face seal groove
	Adapter length	10 mm
	Seal: copper crush washer	ID 4 mm, OD 8 mm, thickness 0.5 mm
Total Assembly	Overall length	$L_n + L_g + L_{casing} - L_g + L_{Nozzle} + L_{Adapter} \approx 175mm$

11. Launcher configurations

11.1. Shoulder-fired tube

A 1 m-long, 30 mm O.D. Inconel 718 SLM tube houses the projectile as shown in **Figure 2a**, weighs ≤ 2.5 kg loaded, and includes a folding stock, pistol grip, iron sights, and built-in setback igniter. Estimated effective range: 500–1500 m; recoil impulse: ~ 15 N·s.

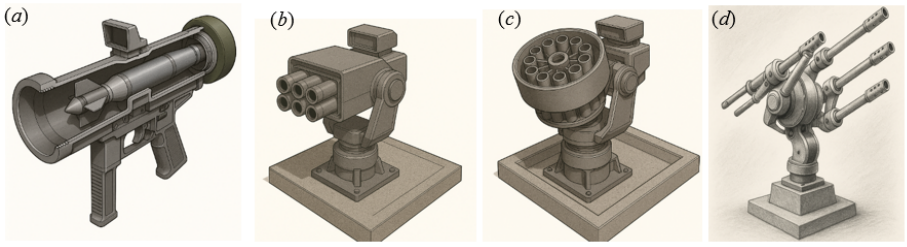

Figure 2. Launcher Assembly Sketch Illustration Configuration: **(a)** Shoulder-Fired Tube; **(b)** Building-Mounted Interceptor; **(c)** Building Mounted Variable-Barrel Cannon Interceptor; **(d)** Building Mounted Variable Moving Cannon Interceptor.

11.2. Building-mounted interceptor

A turreted 12-tube pod (400 × 400 × 1000 mm) with two-axis servo gimbal as shown in **Figure 2b**, radar/EO tracking, and rapid-fire capability intercepts drones, rockets, or low-altitude aircraft at 100–2000 m. Magazine reload enables sustained defense in a networked or standalone "defense cloud."

11.3. Building-mounted variable-barrel cannon interceptor

A next-generation, building-mounted variable-barrel cannon interceptor (**Figure 2c**) comprises a two-axis stabilized turret (Ø600 mm) hosting twelve modular 30 mm launch tubes. Each tube is fixed at a distinct elevation bias (–10° to +60°) and arranged at 30° azimuthal intervals, permitting the fire-control system to select individual barrels or coordinated barrel clusters in real time according to target bearing, elevation and closing velocity. Integrated radar (0.5–2 km range) and electro-optical trackers compute target state (bearing, elevation, speed: 300–1500 m/s) and assign the pre-biased tube whose orientation minimizes time-of-flight, approximately 5 ms at 100 m and 1.4 s at 2 km for a 1400 m/s projectile. By sequencing firings from tubes with differing angles and muzzle velocities the system produces multi-vector engagement profiles that stagger time-of-flight to saturate evasive targets or to optimize impact geometry for penetrating composite and reactive armors. Rotating the firing sequence across the array also moderates thermal and mechanical loading, enabling short cool-down intervals and extended barrel life. The twelve-tube magazine can be expended in 1.2 s (600 rounds/min); distributing shots across the array limits individual barrel heating to below ~150 °C per volley well within Inconel 718 thermal margins, and the turret's slewing capability (150°/s azimuth, 120°/s elevation; $\tau_{90} \approx 0.1$ s) ensures rapid reacquisition. Overall, the design converts a fixed rooftop, vehicle or ship mount into a high-throughput, adaptive defense node capable of engaging threats from small UAS to high-speed anti-ship missiles without the mass, complexity or maintenance burden of a continuously gimbaled, single-barrel system.

11.4. Building-mounted variable moving cannon interceptor

Perched atop a reinforced rooftop plinth, the interceptor exhibited in **Figure 2d** features four independent 20 mm barrels (Ø20.0 mm) arranged in a cruciform layout, each mounted via a three-axis adapter enabling ±45° pitch, ±180° yaw and ±10° roll motion at up to 60°/s. A central actuator rotates the entire assembly through 360° in under 2 s, while each barrel can be sequentially indexed, switching firing lines in ≤0.1 s to maintain a continuous 2400 rounds-per-minute aggregate rate (600 rpm per barrel). With a muzzle velocity of 950 m/s, the system can reliably engage targets at up to 2000 m, predicting intercept points for incoming threats traveling up to Mach 2 (680 m/s) by computing lead angles to within 0.05° accuracy. All kinematics and firing sequences are governed by a real-time fire-control computer, which ingests seeker data and issues barrel-selection commands through high-speed CAN bus links, ensuring precise, high-rate interception of fast-moving aerial or surface threats.

12. Experimental validation plan

This section outlines the experimental campaign designed to validate the principal analytic claims regarding propulsion performance, thermal resilience, and terminal ballistics. The validation strategy utilizes two parallel tracks: component-level laboratory testing and integrated full-system field trials.

12.1. Component and cold-flow test matrix (lab bench)

This stage is composed of the following steps:

(i) *Material coupons and thermal tests:*

a. PEEK, phenolic ablative and Inconel 718 coupons (n = 5 each) exposed to combined convective and radiative heating in an oxy-acetylene/plasma arc rig to reproduce throat heat flux (target peak ≈ 8.0–9.0 MW/m²). Metrics include mass loss, char depth, and tensile strength retention.

b. Temperature instrumentation: k-type thermocouples, IR thermography (frame rate ≥1 kHz). Acceptance metrics: PEEK char depth ≤ 1.5–3.0 mm for 2.5 s pulse in conservative runs; Inconel remaining ductile at test peak temperature (no gross creep or cracking).

(ii) *Cold-flow nozzle testing:*

a. 3D-printed SLM Inconel nozzles will be instrumented to measure wall pressure distribution. Schlieren imaging will verify the supersonic exhaust profile with cold-air compressed flows (scaled mass flow), and ensure the absence of internal shocks under scaled mass-flow conditions.

b. Verify exit Mach and under-expanded condition behavior; validate contour avoids internal shocks.

(iii) *Igniter bench testing:*

a. The mechanical setback device will undergo repetitive testing (reproduce accelerations) on a centrifuge and/or gas gun to verify arming thresholds, primer strike energy, and flash train reliability (≥98% reliability target).

b. Tests include spin-safe torque tests to verify shear ring unscrew thresholds.

12.2. Integrated hot-fire motor tests (controlled test range)

This stage is composed of the following steps:

(i) *Single-shot hot-fire (n ≥ 10):*

a. Instrumentation: onboard pressure transducer, thrust stand, high-speed camera, gas sampling for combustion products.

b. Metrics: chamber pressure trace (target 8 ± 0.6 MPa), thrust curve, total impulse (≈ 300 Ns ± 10%), exit velocity (streak camera or Doppler radar), burn duration ≈ 2.5 s.

(ii) *Thermo-structural post-shot evaluation:* Non-destructive evaluation (NDE) of casing (ultrasound/dye-penetrant), metallography on sacrificial test articles, and liner thickness measurement.

(iii) *Terminal Ballistics:* Live-fire tests using a test barrel or gas-gun hybrid facility (for repeatability) against instrumented RHA blocks and composite panels at

ranges of 100–500 m will quantify penetration depth, residual mass and fragment cloud using high-speed videography and post-impact sectioning validating the hydrodynamic models presented in Section 10. Acceptance criteria are achieved for mean penetration within ±15% of analytic model predictions (target ≈ 116 mm ± 15%).

12.3. High-fidelity numerical verification (parallel)

Concurrent with physical testing, computational fluid dynamics (CFD) using RANS/LES solvers will refine internal Bartz and Nagler ballistic estimates: chamber flow, throat heat flux and expected boundary layer behaviour with a chemical equilibrium gas model. Second step, hydrocode impact simulations (Eulerian/ Lagrangian coupling) will model complex penetration mechanics into multi-layer composite and steel targets (use ALE/SPH tools) to compare with hydrodynamic model.

12.4. Schedule and safety

Staged campaign with initial coupon tests (0–2 months), cold-flow & igniter bench tests (2–4 months), integrated hot-fire and penetration tests (4–8 months), and full numerical verification running in parallel. All tests adhere to appropriate explosives and environmental safety regulations; test sites are selected with containment for combustion products and fragments.

13. Environmental, handling and compatibility analysis

This section assesses the system's lifecycle compatibility, focusing on environmental emissions, material stability, and operational safety, according to the following steps:

(i) *Combustion products and Emissions:* The AP/HTPB propellant generates Hydrogen Chloride (HCl) and particulate chlorine compounds upon decomposition. While the mass fraction for a single miniature motor is low, indoor testing requires active plume scrubbing and ventilation. For field deployment, the rapid atmospheric dilution mitigates acute toxicity; however, future iterations may consider low-smoke or ammonium-nitrate-based formulations to reduce corrosive effluent, subject to specific impulse (I_{sp}) trade-offs.

(ii) *Materials & Corrosion Compatibility:*

a. Inconel 718, while inherently corrosion-resistant, repeated exposure to chloride-rich combustion residues can induce pitting. Naval applications will require sacrificial coatings or post-firing freshwater rinsing protocols.

b. Polymers (PEEK/Phenolic) design storage conditions protocols ≤ 40 °C, dry, and provide UV shielding robust mechanical bonding to prevent delamination over shelf life. Components will undergo humidity and salt-fog testing per MIL-STD-810F standards.

c. Safety & Acoustics: Muzzle blast overpressure mandates operator hearing protection and defined standoff distances. Building-mounted interceptor nodes will incorporate acoustic baffling and blast arrestors. Regarding the "Defense Projectiles Cloud" mode, engagement rules must be strictly

geofenced to manage the dispersion of falling debris in populated (i.e., Urban environments) areas.

(iii) *Logistic & Lifecycle:* To ensure propellant integrity over a 10-year shelf life, projectiles will be sealed in desiccant-equipped canisters with a passive thermal range of −20 °C to +55 °C. All onboard electronics (in guided variants, EMC/EMI) must meet MIL-STD-461 immunity levels for operation in high-electromagnetic environments.

14. Applications in integrated defense architectures

The system offers versatile anti-air and anti-armor capabilities for dismounted infantry, vehicle-mounted installations, rooftop defense, and naval point-defense against UAVs, rockets, and light combat aircraft.

14.1. Anti-air defense combined cannons system

The 20 mm solid rocket projectile and its modular launcher suite are ideally suited for integration into a layered anti-air defense architecture combining fixed, mobile, and soldier-portable units. In this context, the building-mounted interceptors serve as mid-range kinetic barriers for neutralizing drones, loitering munitions, and cruise missiles in urban or base environments, while vehicle-mounted turrets extend coverage to mobile forward-operating zones. The shoulder-fired handheld variant offers a dismounted response for infantry and special forces to target low-altitude aerial threats up to 1.5 km away. Centralized fire-control software fuses radar and EO/IR tracking data to cue the appropriate launcher, whether rooftop, vehicle, or human-carried, selecting the best firing angle, projectile timing, and launcher configuration. This synergy of varied platforms using a unified projectile system simplifies logistics, reduces training burden, and maximizes coverage flexibility across threat profiles.

14.2. Defense projectiles cloud concept

In high-saturation threat environments, such as swarm UAV attacks or simultaneous salvo launches the system supports a “defense projectiles cloud” mode, wherein multiple launch tubes across several distributed platforms fire in coordinated overlapping patterns to saturate airspace with high-speed interceptors. Each 20 mm projectile contributes a focused kinetic ray traveling at 1400 m/s, and when launched in rapid succession from varied azimuths and elevations (using the variable-barrel and moving-cannon interceptors), the collective projectile paths form a volumetric grid or mesh, effectively constructing a dynamic shield zone. This scalable approach enhances the probability of kill (Pk) per volume, creates layered redundancy, and enables wide-area denial to enemy airborne systems using cost-effective unguided interceptors, all coordinated through real-time sensor fusion and predictive targeting algorithms.

14.3. Small-scale maneuverable solid rocket with canards and winglets

A compact, maneuverable rocket variant of the 20 mm solid-propellant projectile shown in **Figure 3** integrates four actuated canards near the nose and four fixed

aerodynamic winglets at the aft section to enable pitch, yaw, and roll control during powered and ballistic flight. The total length of the projectile is 200 mm, with a body diameter of 20 mm and an overall fin span of 60 mm. The control system consists of micro-electromechanical actuators (MEMS) embedded behind the canards, each providing up to ±20° of deflection within 50 ms, enabling dynamic flight vectoring. The solid motor, identical to the base design, produces 300 Ns total impulse over 2.5 s with an average thrust of 120 N, accelerating the 180 g projectile to 1400 m/s. During powered flight, the canards provide up to 10 g lateral acceleration for course correction or target acquisition. The center of pressure is offset 40 mm behind the center of gravity, ensuring inherent static stability, while active control via a small onboard IMU (inertial measurement unit) and pre-programmed trajectory logic enables rapid intercept or path shaping. The winglets serve to stabilize high-speed glide and prevent tumbling after burnout. This configuration extends utility into guided roles such as air-to-air intercepts or smart munitions for close-range precision engagements.

Figure 3. Small-Scale Maneuverable Solid Rocket with Canards and Winglets.

Below is a side-by-side comparison, both quantitative and qualitative of our three launcher concepts (20 mm handheld rocket tube, 20 mm variable-barrel rooftop interceptor, and fixed multi-tube interceptor) against fielded equivalents in light antitank and point-defense roles.

15. Comparative operational assessment of 20 mm rocket-propelled systems

This section is based on **Tables 5** and **6**, quantitative and qualitative data, respectively. The *Hand-Portable Rocket Cannon* delivers armor penetration performance that matches or exceeds that of saboted Armor-Piercing Discarding Sabot (APDS) projectiles, all within a system weighing less than 3 kg. This makes it ideally suited for dismounted infantry roles, particularly in anti-armor operations and medium-altitude drone defense. While it offers excellent lethality with minimal logistical burden, it is limited by a low rate of fire. The *Variable-Barrel Rooftop Interceptor* enables rapid salvo fire (up to 600 rounds per minute) and uses pre-bored elevation offsets to minimize engagement time. It is highly versatile across a range of threats, including unmanned aerial systems (UAS), loitering munitions, and short-range rockets. The *Fixed Multi-Tube Interceptor* provides the highest volume

of fire among the systems discussed, making it effective for counter-rocket, artillery, and mortar (C-RAM) defense against saturation attacks. However, its size and power requirements restrict its use to vehicle-mounted or naval installations.

Table 5. Quantitative Comparison.

Metric/system	20 mm hand-portable rocket cannon	20 mm variable-barrel rooftop	Fixed multi-tube interceptor (ship/veh)	M136 AT4 HEAT	FIM-92 Stinger (SAM)	Phalanx CIWS
Projectile diameter (caliber):	20 mm	20 mm	20 mm	84 mm	70 mm	20 mm
Total projectile mass (nominal):	0.18 kg	0.18 kg	0.18 kg	3.9 kg	15 kg	0.4 kg
Warhead Type	AP/HTPB monoprop	AP/HTPB monoprop	AP/HTPB monoprop	Shaped-charge HEAT	HE-fragmentation	Tungsten AP-FS
Penetration (RHA equiv.)	116 mm	116 mm	116 mm	420 mm @ 0 m	N/A (airburst)	~20 mm (per round)
Engagement Range	0.5–1.5 km	0.1–2.0 km	0.2–2.0 km	300 m	4.5 km	1.5 km
Exit Velocity	1400 m/s	1400 m/s	1400 m/s	290 m/s	750 m/s	1226 m/s
Rate of Fire	Single-shot, 1 r/min	600 r/min (salvo capacity)	600 r/min (12-tube salvo)	Single-shot	Single-shot	4500 r/min
System Mass (loaded)	2.5 kg	50 kg	200 kg	6.7 kg	15 kg	~6500 kg
Mobility	Dismounted soldier	Rooftop fixed	Vehicle/ship-integrated	Dismounted soldier	Dismounted soldier	Ship/installation
Power Requirement	None	500 W	2 kW	None	Battery	500 kW

Table 6. Qualitative Comparison.

Feature	20 mm hand-portable rocket cannon	20 mm variable-barrel rooftop	Fixed multi-tube interceptor	M136 AT4 HEAT	FIM-92 Stinger	Phalanx CIWS
Portability	Excellent (≤ 2.5 kg)	Poor (requires mounting)	Very poor (200 kg, fixed)	Good (6.7 kg tube)	Moderate (15 kg man-portable)	Very poor (ship-borne installation)
Engagement Envelope	Mid-range armor/area	Flexible elevation & range	Long-range, multi-threat	Short-range armor only	Long-range aerial only	Point-defense, very high rate
Warhead Versatility	Low (AP only)	Low (AP only)	Low (AP only)	High (shaped charge)	Moderate (HE/fragmentation)	Low (kinetic)
Rate-of-Fire Flexibility	Single-shot	Configurable salvo patterns	High sustained bursts	Single-shot	Single-shot	Very high
Thermal & Logistic Footprint	Minimal	Moderate (requires power)	High (power + cooling)	Minimal	Minimal	High (power cooling, ammo supply)
Counter-UAS Capability	Fair (fast, small drone)	Excellent (rapid, multi-vector)	Excellent (volume fire)	Poor	Excellent	Excellent
Counter-Rocket/ Artillery	Fair (guided)	Good (salvo spill-over)	Excellent (pure volume)	Poor	Poor	Moderate
Ease of Integration	Plug-and-play tube	Requires rooftop structure	Requires heavy installation	Tube replacement	Minimal training	Platform integration
Cost per Round	Moderate	Moderate	Low (bulk)	High (shaped charge)	Very high (guided missile)	Low (unguided)

15.1. Comparison with existing defense systems

AT4 offers superior single-shot armor penetration; however, due to its short range and heavy warhead, its adaptability and portability are reduced. Moreover, *Stinger Missile* excels in range and guidance against aircraft, although it is cost-prohibitive for mass use, especially against drone swarms or small threats. Finally, *Phalanx CIWS* unmatched in rate of fire for close-in defense, is on the other hand limited in lethality against heavily armored targets due to its kinetic-only profile.

15.2. Capability positioning

Together, these 20 mm rocket-propelled systems bridge the gap between lightweight infantry anti-tank weapons and high-volume point-defense guns. They offer (i) Moderate armor penetration, (ii) Extended engagement range, (iii) Low cost per engagement and (iv) Deployment flexibility across portable, rooftop, and mounted platforms. These systems provide a scalable, cost-effective response to modern battlefield threats such as light armor, drones, and loitering munitions, while maintaining a low logistical footprint suitable for both conventional and asymmetric operational environments.

16. Conclusion

This study has presented a comprehensive analytical framework for the design, evaluation, and application of a high-speed, 20 mm rocket-propelled projectile system, incorporating solid propulsion, thermal protection, mechanical arming, and multi-platform launch configurations. Through rigorous modeling of internal ballistics, nozzle flow, thermal-structural response, and boundary-layer dynamics, the projectile system has demonstrated the potential to achieve sustained supersonic flight at Mach 4 with reliable ignition and effective structural resilience under combustion and aerodynamic loading.

The integration of a mechanically-armed, pyrotechnic ignition mechanism ensures autonomous operation upon muzzle exit, eliminating the need for external firing infrastructure and enabling compact, self-contained operation across all launch platforms. Thermal analyses confirmed that the selected combination of Inconel 718 structural casing and PEEK insulation, complemented by optional ablative phenolic liners, provides sufficient protection against peak heat fluxes up to 8.8 MW/m², ensuring survivability of internal components during both launch and flight.

The projectile's penetration capability, derived from hydrodynamic and empirical models, exceeds 100 mm RHA equivalent and up to 140 mm in modern composite laminates, validating its utility in both anti-armor and anti-air roles. Comparative analysis with existing systems highlights the favorable balance this platform achieves between performance, size, and cost; positioning it between man-portable anti-tank weapons and high-volume point-defense systems such as CIWS.

Furthermore, the modular launcher configurations, ranging from handheld tubes to fixed rooftop arrays and advanced variable-barrel interceptors demonstrate the scalability and operational flexibility of the system. These configurations enable deployment in diverse mission scenarios including urban air defense, vehicular integration, and saturation countermeasure environments.

Overall, the work establishes a novel concept in miniature, high-performance rocket munitions capable of addressing contemporary defense challenges, particularly those posed by fast-moving, lightly armored aerial and ground threats. The analytical results support the feasibility of this system and serve as a foundation for future experimental validation and system-level integration within layered defense architectures.

Funding: This research has no funding source.

Institutional review board statement: Not applicable.

Informed consent statement: Not applicable.

Data availability statement: Not applicable.

Conflict of interest: The author declares that he has no conflict of interest.

References

1. Jasper S. Resilience Against Hybrid Threats: Empowered by Emerging Technologies: A Study Based on Russian Invasion of Ukraine. In: Balomenos KP, Fytopoulos A, Pardalos PM (editors). Handbook for Management of Threats, Springer Optimization and Its Applications. Springer International Publishing; 2023. pp. 209–226. doi: 10.1007/978-3-031-39542-0_10
2. Sutton GP, Biblarz O. Rocket propulsion elements, 9th ed. John Wiley & Sons; 2016.
3. Khalil M, Ahmed MYM. Flight Performance and Dispersion Analysis for a Flexible Tactical Missile. Journal of Spacecraft and Rockets. 2023; 60(4): 1297–1307. doi: 10.2514/1.A35607
4. Defense Science Board Task Force on Directed Energy Weapons. Available online: https://dsb.cto.mil/wp-content/uploads/reports/2000s/ADA476320.pdf (accessed on 1 January 2025).
5. Remissa I, Jabri H, Hairch Y, et al. Propulsion Systems, Propellants, Green Propulsion Subsystems and their Applications: A Review. Eurasian Chemico-Technological Journal. 2023; 25(1): 3–19. doi: 10.18321/ectj1491
6. Thomas DJ. Advanced 3D additive manufacturing techniques for revolutionizing the next-generation rocket engine nozzle fabrication. The International Journal of Advanced Manufacturing Technology. 2023; 127(7–8): 3747–3760. doi: 10.1007/s00170-023-11669-7
7. Denny M, McFadzean A. Rocket Science: From Fireworks to the Photon Drive. Springer International Publishing; 2019. doi: 10.1007/978-3-030-28080-2
8. Wu H, Hou Y, Yang L. A Multi-Interaction Filtering Control Game Model for Close-in Shipborne Gun Weapon System. In: Proceedings of the 2024 International Conference on Machine Intelligence and Digital Applications; 30 May 2024; Ningbo, China. pp. 750–755. doi: 10.1145/3662739.3665688
9. Li J, Mei Z, Shen Q, et al. Analysis on Core Capabilities and Key Technologies of Future Air Defense Anti-missile Operations. In: Long S, Dhillon BS (editors). Man-Machine-Environment System Engineering, Lecture Notes in Electrical Engineering. Springer; 2020. 645, pp. 1047–1054. doi: 10.1007/978-981-15-6978-4_120
10. Lyu C, Zhan R. Global Analysis of Active Defense Technologies for Unmanned Aerial Vehicle. IEEE Aerospace and Electronic Systems Magazine. 2022; 37(1): 6–31. doi: 10.1109/MAES.2021.3115205
11. Pecht E, Tishler A, Weingold N. On the choice of multi-task r&d defense projects: A case study of the israeli missile defense system. Defence and Peace Economics. 2013; 24(5): 429–448. doi: 10.1080/10242694.2012.717205
12. Hartlage B, Owen M, Frederick R, et al. Enhanced Counter Air Projectile. In: Proceedings of the 40th AIAA/ASME/SAE/ASEE Joint Propulsion Conference and Exhibit; 11 July 2004; Fort Lauderdale, FL, USA. doi: 10.2514/6.2004-4086
13. Williams J, Brekke K, Patrick S, et al. Conceptual Design of a Guided Interceptor. In: Proceedings of the 41st AIAA/ASME/SAE/ASEE Joint Propulsion Conference & Exhibit; 10 July 2005; Tucson, AZ, USA. doi: 10.2514/6.2005-3847
14. Fletcher JC. The technologies for ballistic missile defense. Issues in Science and Technology. 1984; 1(1): .29–15 Available online: www.jstor.org/stable/43308851
15. Önder A. Projectile fragmentation and debris cloud formation behaviour of wavy plates in hypervelocity impact. International Journal of Impact Engineering. 2024; 183: 104788. doi: 10.1016/j.ijimpeng.2023.104788
16. Abdulhamid H, Mespoulet J, Deconinck P. On The Effect of Projectile Material on Damage Induced to Single and Multi-Plate Target. In: Proceedings of the 2024 17th Hypervelocity Impact Symposium; 13 September 2024; Tsukuba, Japan. doi: 10.1115/HVIS2024-106
17. Abdulhamid H, Mespoulet J, Deconinck P. On the effect of projectile material on damage induced to aluminum target under hypervelocity impact. International Journal of Impact Engineering. 2025; 202: 105326. doi: 10.1016/j.ijimpeng.2025.105326
18. Xue Y, Zhang Q, Hao W, et al. Energy distribution characteristic of impact flash of metallic target impacted by hypersonic projectile. International Journal of Impact Engineering. 2024; 186: 104866. doi: 10.1016/j.ijimpeng.2023.104866
19. Zong H-Z, Xu H-M, Zhang S-K, et al. A Review of the Application of Al/PTFE Reactive Materials in Damage and Defense Applications. Journal of Energetic Materials. 2025; 1–36. doi: 10.1080/07370652.2025.2495554
20. Liu Z, Wu Q, Gao H, et al. Enhancing Whipple shield defense against hypervelocity impacts: Influence of impactor geometry and surface treatments. Advances in Space Research. 2025; 76(3): 1674–1691. doi: 10.1016/j.asr.2025.05.041

21. Williams P, Vinnikova S, Ahmed I, et al. Orbital Debris Cloud Propagation Simulation in Orbit. In: Proceedings of the AIAA Aviation Forum and ASCEND 2025; 29 July 2025; Las Vegas, NA, USA. doi: 10.2514/6.2025-4007
22. Peng XF, Xiang H, Liang JY, et al. Simulation and experimental analysis of explosive reactive armor collateral damage. Journal of Physics: Conference Series. 2024; 2891(4): 042007. doi: 10.1088/1742-6596/2891/4/042007
23. Shu P, Zhao M, Li Z-Y, et al. Short-term evolution and risks of debris cloud stemming from collisions in geostationary orbit. Acta Astronautica. 2025; 228: 486–493. doi: 10.1016/j.actaastro.2024.12.016
24. Tian W, Du W, Zhang Z, et al. Experimental Investigation of Reaction-Induced Pressure Perturbations in PTFE/Al Composites During Shock Compression. Materials. 2025; 18(18): 4267. doi: 10.3390/ma18184267
25. Veraar RG, Oosthuisen R, Andersson K. Ramjet Propulsion for Projectiles: An Overview of Worldwide Achievements and Future Opportunities. International Journal of Energetic Materials and Chemical Propulsion. 2022; 21(5): 1–61. doi: 10.1615/IntJEnergeticMaterialsChemProp.2022038741
26. Research Project Report Investigation of a Solid Fuel Ramjet Projectile. Available online: https://aerospace.technion.ac.il/wp-content/uploads/2024/08/project-Itamar-Levitan-final.pdf (accessed on 1 January 2025).
27. Nagler J. On Thermoelastic Impact Modelling of Frozen Composite Target During Pre – Heated Projectile Penetration Starts of Motion. PROOF. 2024; 4: 26–68. doi: 10.37394/232020.2024.4.4
28. Patel P, Hull TR, McCabe RW, et al. Mechanism of thermal decomposition of poly (ether ether ketone) (PEEK) from a review of decomposition studies. Polymer Degradation and Stability. 2010; 95(5): 709–718. doi: 10.1016/j.polymdegradstab.2010.01.024
29. Solution of the Boundary Layer Equations for a Rotating Cone in Supersonic Flow. Available online: https://aerospace.technion.ac.il/wp-content/uploads/2024/11/Shahaf_Haiman-PROJECT.pdf (accessed on 1 January 2025).
30. Shock-Fitting Computational Method for the Inviscid Blunt-Body Problem. Available online: https://aerospace.technion.ac.il/wp-content/uploads/2023/11/Shock-Fitting-Computational-Method-for-the-Inviscid-Blunt-Body-Problem-%D7%90%D7%99%D7%9C%D7%99%D7%94-%D7%9E%D7%99%D7%9C%D7%9E%D7%9F.pdf (accessed on 1 January 2025).